Available online at www.sciencedirect.com
ScienceDirect
Journal of Sound and Vibration 303 (2007) 440–454
JOURNAL OF SOUND AND VIBRATION
www.elsevier.com/locate/jsvi

Rotordynamical modelling of a fibre refiner during production

M. Karlberg*, J.-O. Aidanpää

Department of Applied Physics and Mechanical Engineering, Division of Computer Aided Design, Luleå University of Technology, SE-97187 Luleå, Sweden

Received 11 August 2005; received in revised form 4 September 2006; accepted 8 November 2006
Available online 27 March 2007

Abstract

A key component in panel board production is the fibre refiner, whose task is to break cellulose wood chips into slender fibres. This refining process takes place between a rotor and a stator, where a gap of around 0.5 mm is found. In the development of these refiners predicting the dynamics is important; hence, mathematical models are needed. For refiners and other applications like brakes, turbines, and compressors, the interaction between the rotor and the surrounding medium can in many situations be significant. In addition to external load, this interaction can also change the characteristics of the system, which should be considered in the design process. Today, there exists no validated load model for fibre refiner process. Hence, the aim of this paper is to suggest one.

Measured axial force data were divided into a constant part and a superimposed oscillating part with different frequencies. For both parts a linear dependence on the gap between the stator and the rotor was assumed. Finally, a four degrees of freedom (dof) model was used to fit a pressure distribution to the axial force model.

This process load model led to stiffness and external loads that can be both time dependant. If the pressure distribution only shows a radial variation along the refining zone, all the external loads except the axial one will vanish. The number of functions describing the stiffness parameters also decrease from eight to four. In one case, four stiffness coefficients vanish, whereas the remaining coefficients become constant. This occurs if the process load does not follow the angular vibrations and there is no gap dependence on the oscillating parts of the process load. Numerical simulations showed that by applying a specific process load model, the vibration orbit changed from the unbalance response by means of shape and vibration origin. The unstable domain was further increased when the process load model was applied.

Measurements are necessary to select a realistic process model for a specific application. The derived model can be used in product development to choose suitable system parameters and thus to avoid dynamical problems.
© 2006 Elsevier Ltd. All rights reserved.

1. Introduction

A key component in panel board production is the fibre refiner (an overhung rotor), whose task is to break cellulose wood chips into slender fibres. Because the fibre refiner is driven by an electrical motor, the operating spin speed is 25 or 30 Hz depending on the frequency of the electrical grid. Rotordynamics are essential when developing new fibre refiners, since vibrations can cause serious damage. To predict the dynamics, mathematical models are needed. For simplicity the system is often assumed linear with constant coefficients

*Corresponding author.
E-mail address: magkar@ltu.se (M. Karlberg).

0022-460X/$ - see front matter © 2006 Elsevier Ltd. All rights reserved.
doi:10.1016/j.jsv.2006.11.021

Nomenclature

a_1–a_4 constants
C centre of the rotor
$\mathbf{C}$ damping matrix
F_{pX}, F_{pY}, F_{pZ} process forces
F_{pZs} constant part of the axial process force
F_{pZo} oscillating part of the axial process force
f_{pX}, f_{pY}, $f_{p\varphi}$, $f_{p\theta}$ process load coefficients
$\mathbf{f}_p$ process load vector
$\mathbf{F}_r$ restoring load vector
$\mathbf{f}_u$ unbalance load vector
J_p polar moment of inertia
J_t transversal moment of inertia
k_{11}, k_{12}, k_{21}, k_{22} structure stiffness coefficients
k_{p1}–k_{p8} process stiffness coefficients
$\mathbf{K}_s$ stiffness matrix due to the structure
$\mathbf{K}_p$ stiffness matrix due to the process
M_{pX}, M_{pY}, M_{pZ} process moments
m rotormass
$\mathbf{M}$ mass matrix
O origin of fixed frame
p pressure in refining zone
P point on rotor
r radial coordinate on the rotor
r_1, r_2 inlet and outlet radius
$\mathbf{R}_1$, $\mathbf{R}_2$ transformation matrices
s gap between stator and rotor at a certain position on the rotor
s_{nom} nominal gap, i.e. gap between centre of rotor and stator
t time
x, y translational dof in a frame following the angular vibrations
$\mathbf{X}$ vector of generalised coordinates
X, Y translational dof in fixed frame
α, β proportional damping constants
γ_1, γ_2 constants for the stationary part of axial process force measurement
$\gamma_{3(i)}$, $\gamma_{4(i)}$ constants for the oscillating parts of axial process force measurement
δ_c common pressure distribution function
δ_1, δ_2 pressure distribution functions for the stationary part
$\delta_{3(i)}$, $\delta_{4(i)}$ pressure distribution functions for the oscillating parts
ε eccentricity
η angular coordinate on the rotor
θ, φ rotational dof in fixed frame
μ friction coefficient
ω_i ith process frequency
σ_i ith undamped eigenfrequency
ζ_i damping ratio of ith mode
Ω spin speed

Subscripts

i counter
n number of frequency components included

Superscripts

$\wedge$ indication of scaled variable

and with unbalance as the external load. Design calculations such as Campbell diagrams and critical speeds are then a straightforward procedure [1].

One issue about this method is that the rotor interaction with the medium between the stator and rotor in fibre refiners, as well as in other systems like breaks, turbines, and compressors, can be even more important for the dynamics than the unbalance. This load can also be state dependant, meaning that the system characteristics change.

This kind of interaction was studied by Sinou et al. [2], who used a model that changes the stiffness of the system to illustrate how complicated motion can be expected for certain parameter ranges. Destabilising Alford forces is another example that have been studied, for instance in turbines [3] and compressors [4–6]. Few publications concern the process load in fibre refiners, possibly because material modelling is difficult due to the presence of all three phases (gas, liquid and solid material) in the fibre refining process [7]. Certain properties of the material in the refining zone have been characterised [8–11]. However, there exists no validated material model for the refining process, including all three phases to be implemented in a simulation programme at a macro-level. For this reason, different assumptions on the process load were made to study the different phenomena. Whalley and Mitchell [12], for example, studied the torsion vibration of a twin stator disc refiner setup, where the process was assumed to lead to a friction force that varied with a certain pulsating

frequency. This model does not include the flexural degrees of freedom (dof) and hence cannot be used to discuss the effects of a process gap dependency between rotor and stator. Frazier [13] used a hydrodynamic lubrication model for the process load to show how the thrust load depends on the gap between the stator and rotor. Jiang and Yu [14] studied lateral vibrations of a rotor-bearing system with hydrodynamic thrust bearing, demonstrating how such thrust bearing can be used to increase the critical speeds. Ouellet and Weiss [15] studied nonlinear axial vibrations with an assumed viscoelastic behaviour of the pulp in the refining zone.

Efforts have been made to measure directly in the refining zone. The environment in the refining zone is harsh on measuring equipment, but some results have still been found, e.g. measurements of the shear force, normal force and temperature variations [16–18].

The approach throughout this paper is to use measured data of the axial force to justify a mathematical model for the process inside the refining zone. The parameters included in this model will depend on numerous process parameters, e.g. dilution of water, raw material and type of segments. The objective of this paper is to derive and implement a time- and displacement-dependant process load model and to indicate how such a model can affect the dynamics.

2. Derivation of a model for the axial process load

Measurements on industrial machines were conducted to justify a mathematical model of the refining process. The measurements were carried out on a single-disc refiner working with an approximate power of 5MW in production. Fig. 1 shows the time history of the axial bearing force in the shaft, when the nominal gap (s_{nom}) between the centre of the stator and the rotor is constant. The sign "$\wedge$"indicates that the variables have been scaled and maintained throughout the entire paper. Although the numerical data in the x-domain are not printed in Figs. 1–3, the scale is linear in all figures. These figures are constructed this way because simply motivating how the model is derived is not enough. The signal in Fig. 1 can be represented by a constant part (F_{pZs}) together with an oscillating part (F_{pZo}).

Hence, the axial process force is hence assumed to be

$$F_{pZ} = F_{pZs} + F_{pZo}. \tag{1}$$

The markers in Fig. 2 show how the constant part of the measured axial process force varies with the nominal gap.

Assuming a linear dependency of the nominal gap gives,

$$F_{pZs} = -\gamma_1 + \gamma_2 s_{\text{nom}} \tag{2}$$

for the constant axial process force, where γ are constants. The solid black line in Fig. 2 is given by Eq. (2), where the parameters have been fitted to match the measured data.

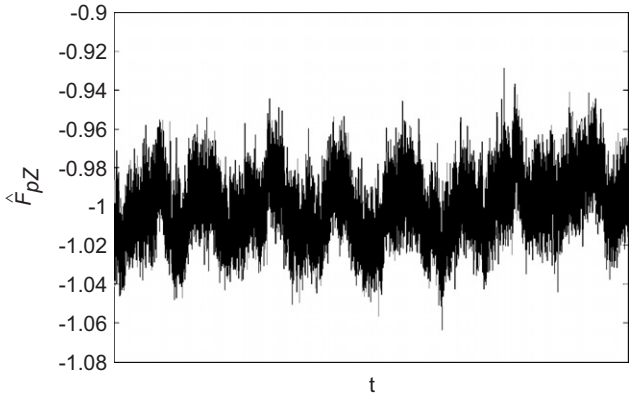

Fig. 1. Time history of bearing force.

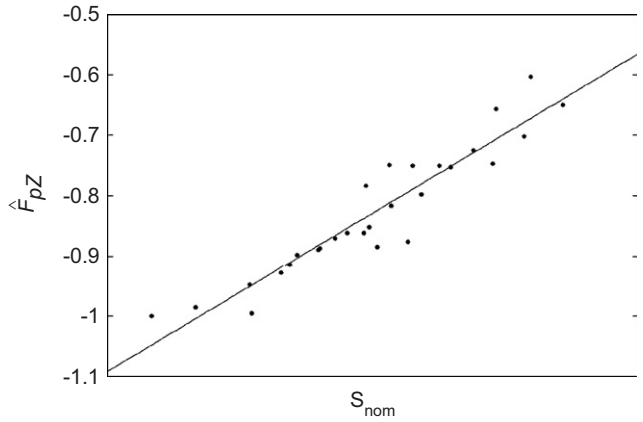

Fig. 2. Constant axial process force as function of the nominal gap.

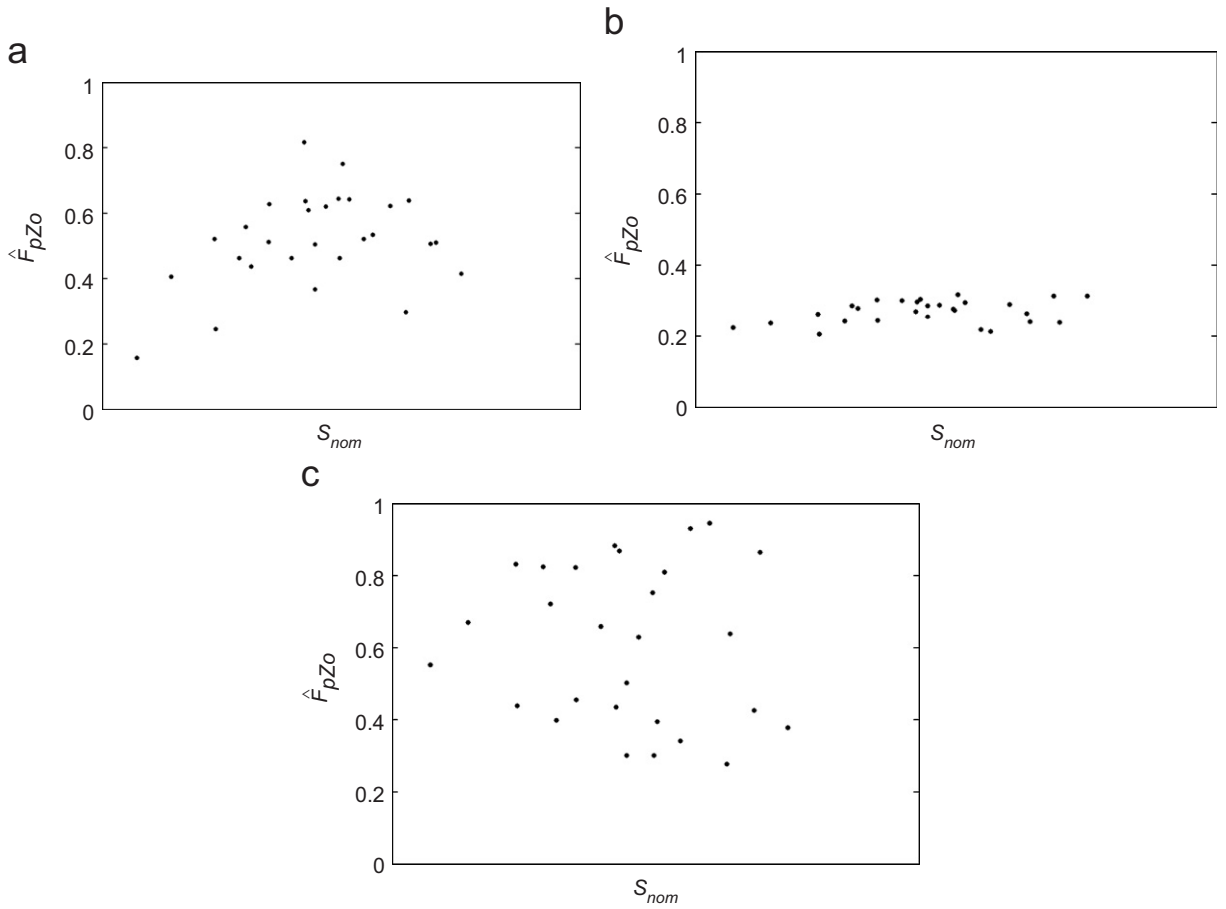

Fig. 3. Discrete Fourier transform amplitude of the oscillating axial process force for (a) the low-, (b) middle- and (c) high frequency components.

Fig. 3 shows the resulting DFT-amplitude (square root of sine and cosine components) as a function of the nominal gap for three frequencies. The amplitudes are shown in Fig. 3(a) (lowest frequency component of the three), Fig. 3(b) (medium frequency component) and Fig. 3(c) (highest frequency component).

Fig. 3 does not indicate if the oscillating part depends on the nominal gap. If a nominal gap dependency of the oscillating parts exists, it is assumed to be linear. This is assuming

$$F_{pZo} = \sum_{i=1}^{n} (-\gamma_{3(i)} + \gamma_{4(i)} s_{\text{nom}}) \cos(\omega_i t) \tag{3}$$

for the oscillating part, where γ are constants, ω_i is the ith frequency component and n is the number of frequency components to be used. Inserting Eqs. (2) and (3) into Eq. (1) gives

$$F_{pZ} = -\gamma_1 + \gamma_2 s_{\text{nom}} + \sum_{i=1}^{n} (-\gamma_{3(i)} + \gamma_{4(i)} s_{\text{nom}}) \cos(\omega_i t) \tag{4}$$

for the axial process force.

3. Process models in the refining zone and their coupling to the axial process force

This paper hypothesises that the process can be treated as a displacement-dependant pressure, which together with a frictional coefficient affects the dynamics of the system. However, after integration over the active area no unique pressure distribution fits the axial process force given by Eq. (4), though infinite possibilities exist.

3.1. The rotordynamical model

To derive a load model of the refining process, the rotordynamical model used must be defined. The refiner is considered to be a rigid 4 dof body supported by a bearing structure with linear stiffness. X and Y in the **i** and **j** directions are the translational dof, while φ and θ are the rotational dof about these axes (see Fig. 4). The Cartesian coordinate system $OXYZ$ is fixed in space and the point C is attached to the geometrical centre of the rotor. When the machine is running on idle and subjected to unbalance, the corresponding equation of motion can be written as [19]

$$\mathbf{M}\ddot{\mathbf{X}} + (\mathbf{C} + \Omega\mathbf{G})\dot{\mathbf{X}} + \mathbf{K}_s\mathbf{X} = \mathbf{f}_u(t), \tag{5}$$

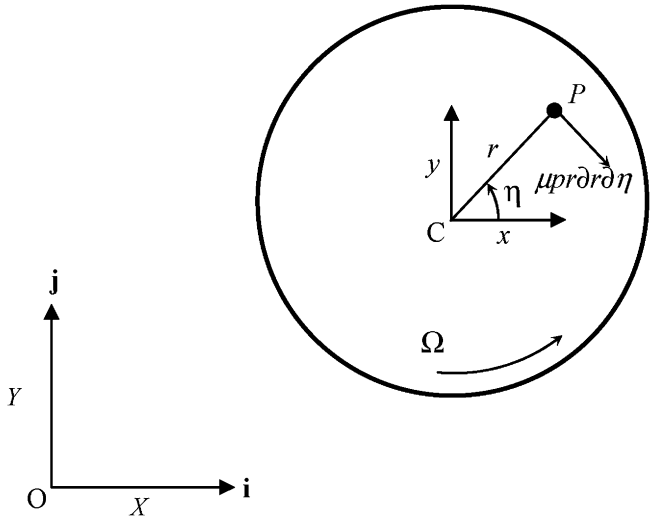

Fig. 4. Model of the refiner.

where

$$\mathbf{M}=\begin{bmatrix} m & 0 & 0 & 0 \\ 0 & m & 0 & 0 \\ 0 & 0 & J_t & 0 \\ 0 & 0 & 0 & J_t \end{bmatrix}, \quad \mathbf{K}_s=\begin{bmatrix} k_{11} & 0 & 0 & -k_{12} \\ 0 & k_{11} & k_{12} & 0 \\ 0 & k_{21} & k_{22} & 0 \\ -k_{21} & 0 & 0 & k_{22} \end{bmatrix}, \quad \mathbf{G}=\begin{bmatrix} 0 & 0 & 0 & 0 \\ 0 & 0 & 0 & 0 \\ 0 & 0 & 0 & J_p \\ 0 & 0 & -J_p & 0 \end{bmatrix},$$

$$\mathbf{C}=\alpha\mathbf{M}+\beta\mathbf{K}_s, \quad f_u=[\,m\varepsilon\,\Omega^2\cos(\Omega t) \quad m\varepsilon\,\Omega^2\sin(\Omega t) \quad 0 \quad 0\,]^{\mathrm{T}} \text{ and } \mathbf{X}=[\,X \quad Y \quad \varphi \quad \theta\,]^{\mathrm{T}}. \tag{6-11}$$

The mass of the rotor is denoted m, the transversal/polar mass moment of inertia J_t/J_p, and the structural stiffness coefficients are denoted k_{ij}. The spin speed is denoted Ω, eccentricity ε and $\mathbf{f}_u$ is the corresponding unbalance load. Proportional damping is applied where the constants α and β are coupled to the two undamped eigenfrequencies (σ_1 and σ_2) at standstill, according to

$$\zeta_i=\frac{\alpha}{2\sigma_i}+\frac{\beta\sigma_i}{2} \quad (i=1,2), \tag{12}$$

where $|\sigma_1|<|\sigma_2|$ and ζ_i is the damping ratio of the ith mode.

When the process is treated as a pressure it will act normal to the rotor front surface, i.e. it follows the angular vibrations. To obtain the forces and moments in the fixed frame (**X**), a transformation matrix from a frame coupled to the vibrations has to be defined.

The Cartesian coordinate system Cxyz in Fig. 4 follows the rotational dof, but not the spin. (r, η) are polar coordinates in the xy-plane, μ the friction coefficient and Ω the spin speed. The relation between the two Cartesian systems is given by [19]

$$\begin{Bmatrix} X \\ Y \\ Z \end{Bmatrix}=\begin{Bmatrix} X_C \\ Y_C \\ Z_C \end{Bmatrix}+\mathbf{R}_1^{\mathrm{T}}\mathbf{R}_2^{\mathrm{T}}\begin{Bmatrix} x \\ y \\ z \end{Bmatrix}, \tag{13}$$

where

$$R_1=\begin{bmatrix} 1 & 0 & 0 \\ 0 & \cos(\varphi) & \sin(\varphi) \\ 0 & -\sin(\varphi) & \cos(\varphi) \end{bmatrix} \text{ and } R_2=\begin{bmatrix} \cos(\theta) & 0 & -\sin(\theta) \\ 0 & 1 & 0 \\ \sin(\theta) & 0 & \cos(\theta) \end{bmatrix}. \tag{14,15}$$

The Coulomb friction model is used in this paper. For simplicity the direction of the friction force is assumed to be opposite to the spin at every point P (see Fig. 4), i.e. the model considers neither the whirling nor the process stream for the direction of the shear force.

The resulting forces and moments due to a pressure p and friction μ can be expressed in the $OXYZ$ coordinate as

$$\begin{Bmatrix} F_{pX} \\ F_{pY} \\ F_{pZ} \end{Bmatrix}=\mathbf{R}_1^{\mathrm{T}}\mathbf{R}_2^{\mathrm{T}}\begin{Bmatrix} \int_0^{2\pi}\int_{r_1}^{r_2}\mu\cdot p\cdot r\cdot\sin(\eta)\partial r\,\partial\eta \\ -\int_0^{2\pi}\int_{r_1}^{r_2}\mu\cdot p\cdot r\cdot\cos(\eta)\partial r\,\partial\eta \\ -\int_0^{2\pi}\int_{r_1}^{r_2}p\cdot r\partial r\,\partial\eta \end{Bmatrix} \tag{16}$$

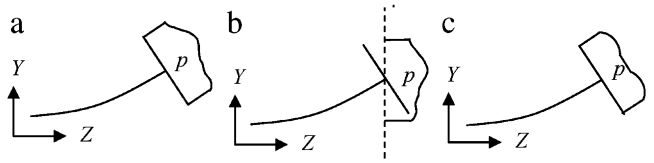

Fig. 5. Load models with: (a) general pressure distribution; (b) distributed spring; and (c) radial pressure distribution.

$$\begin{Bmatrix} M_{pX} \\ M_{pY} \\ M_{pZ} \end{Bmatrix} = \mathbf{R}_1^{\mathrm{T}}\mathbf{R}_2^{\mathrm{T}} \begin{Bmatrix} -\int_0^{2\pi}\int_{r_1}^{r_2} pr^2 \sin(\eta)\partial r\,\partial\eta \\ \int_0^{2\pi}\int_{r_1}^{r_2} pr^2 \cos(\eta)\partial r\,\partial\eta \\ -\int_0^{2\pi}\int_{r_1}^{r_2} \mu p r^2 \partial r\,\partial\eta \end{Bmatrix}, \tag{17}$$

where r_1 is the inlet radius and r_2 the outlet radius of the refining zone.

3.2. Load models

Four different load model cases will be discussed here, using three different ways of dealing with the pressure distribution.

The pressure in Fig. 5(a) is allowed to vary on any point on the rotor, here termed "general pressure distribution". In Fig. 5(b) the general pressure distribution is supposed to work as "distributed springs", i.e. the pressure acts only in the Z-direction. In Fig. 5(c) the angular pressure variations are excluded; this case is referred to as "radial pressure distribution".

3.2.1. Derivation of the load model with general pressure distribution

As shown in the measurements [16], the shear force depends on the radius. Assuming a constant friction coefficient, the pressure must also depend on the radius. This model should also be able to handle variations in circumference (see Fig. 5(a)). Since the pressure should also give rise to a resulting axial force equivalent to the axial process force derived by the measurements (see Eq. (4)), these assumptions result in a proposed pressure distribution

$$p = (\delta_1(r,\eta) - \delta_2(r,\eta)s) + \left(\sum_{i=1}^{n}(\delta_{3(i)}(r,\eta) - \delta_{4(i)}(r,\eta)s)\cos(\omega_i t)\right), \tag{18}$$

where

$$s = s_{\mathrm{nom}} + r(\cos(\varphi)\sin(\theta)\cos(\eta) - \sin(\varphi)\sin(\eta)) \tag{19}$$

and δ is any suitable function of r and η. Assuming small angles of the vibrations, inserting Eqs. (18) and (19) into Eq. (16) gives,

$$\begin{aligned} F_{pZ} = & -\int_0^{2\pi}\int_{r_1}^{r_2} r\delta_1(r,\eta)\partial r\,\partial\eta + \left(\int_0^{2\pi}\int_{r_1}^{r_2} r\delta_2(r,\eta)\partial r\,\partial\eta\right)s_{\mathrm{nom}} \\ & -\int_0^{2\pi}\int_{r_1}^{r_2}\sum_{i=1}^{n} r(\delta_{3(i)}(r,\eta) - \delta_{4(i)}(r,\eta)s_{\mathrm{nom}})\cos(\omega_i t)\partial r\,\partial\eta. \end{aligned} \tag{20}$$

Eq. (20) must be able to fit the axial process force given by Eq. (4). Collecting equal terms by comparing these equations gives,

$$\gamma_1 = \int_0^{2\pi}\int_{r_1}^{r_2} r\delta_1(r,\eta)\partial r\,\partial\eta, \quad \gamma_2 = \int_0^{2\pi}\int_{r_1}^{r_2} r\delta_2(r,\eta)\partial r\,\partial\eta,$$
$$\gamma_{3(i)} = \int_0^{2\pi}\int_{r_1}^{r_2} r\delta_{3(i)}(r,\eta)\partial r\,\partial\eta \quad \text{and} \quad \gamma_{4(i)} = \int_0^{2\pi}\int_{r_1}^{r_2} r\delta_{4(i)}(r,\eta)\partial r\,\partial\eta. \tag{21–24}$$

This means that constants within the functions δ must be chosen so that Eqs. (21)–(24) are fulfilled. Inserting Eqs. (18) and (19) into Eqs. (16) and (17), together with the further assumption of small angles gives,

$$-F_{pX} = k_{p1}\varphi + k_{p2}\theta - f_{pX}, \tag{25}$$

$$-F_{pY} = k_{p3}\varphi + k_{p4}\theta - f_{pY}, \tag{26}$$

$$-M_{pX} = k_{p5}\varphi + k_{p6}\theta - f_{p\varphi}, \tag{27}$$

$$-M_{pY} = k_{p7}\varphi + k_{p8}\theta - f_{p\theta}. \tag{28}$$

The stiffness coefficients ($k_{p1} - k_{p8}$) as well as the external loads ($f_{pX}, f_{pY}, f_{p\varphi}, f_{p\theta}$) are given in Appendix A. These expressions shows that the general pressure distribution gives rise to a time-dependant stiffness matrix,

$$\mathbf{K}_p(t) = \begin{bmatrix} 0 & 0 & k_{p1} & k_{p2} \\ 0 & 0 & k_{p3} & k_{p4} \\ 0 & 0 & k_{p5} & k_{p6} \\ 0 & 0 & k_{p7} & k_{p8} \end{bmatrix} \tag{29}$$

together with an external load vector (i.e. loads independent of the state of the system),

$$\mathbf{f}_p = [f_{pX} \quad f_{pY} \quad f_{p\varphi} \quad f_{p\theta}]^{\mathrm{T}}. \tag{30}$$

The torsion moment becomes

$$M_{pZ} = -\mu \int_0^{2\pi} \int_{r_1}^{r_2} \left(\delta_1(r,\eta) + \delta_2(r,\eta) s_{\mathrm{nom}} - \sum_{i=1}^{n} (\delta_{3(i)}(r,\eta) - \delta_{4(i)}(r,\eta) s_{\mathrm{nom}}) \cos(\omega_i t) \right) r^2 \partial r \, \partial \eta, \tag{31}$$

which can be used to fit the power of the machine.

3.2.2. Derivation of a distributed spring load model

For the above analysis, the process was treated as a pressure so that the direction of the resulting forces and moments then follow the angular vibration. If, however, the process is treated as distributed springs (see Fig. 5(b)) only acting in the Z direction, the transformation matrices become unit matrices. From these assumptions, the stiffness coefficients are

$$k_{p2} = \mu \int_0^{2\pi} \int_{r_1}^{r_2} \left(\delta_2(r,\eta) + \sum_{i=1}^{n} \delta_{4(i)}(r,\eta) \cos(\omega_i t) \right) r^2 \sin(\eta) \cos(\eta) \partial r \, \partial \eta, \tag{32}$$

$$k_{p3} = k_{p2}, \tag{33}$$

$$k_{p6} = -\int_0^{2\pi} \int_{r_1}^{r_2} \left(\delta_2(r,\eta) + \sum_{i=1}^{n} \delta_{4(i)}(r,\eta) \cos(\omega_i t) \right) r^3 \cos(\eta) \sin(\eta) \partial r \, \partial \eta, \tag{34}$$

$$k_{p7} = k_{p6}, \tag{35}$$

while all other coefficients remain unaffected. Notice that neither $\delta_1(\gamma, \eta)$ nor $\delta_3(\gamma, \eta)$ appear in the stiffness matrix, which has been reduced to six coefficients. The external load vector remains unaffected by these assumptions, i.e. given by Eqs. (A.9)–(A.12).

3.2.3. Derivation of the load model with only radial pressure distribution

If the variation along the circumference (η) is negligible compared to the variations along the radius of the rotor, the pressure distribution is

$$p = (\delta_1(r) - \delta_2(r)s) + \left(\sum_{i=1}^{n}(\delta_{3(i)}(r) - \delta_{4(i)}(r)s)\cos(\omega_i t)\right). \tag{36}$$

The stiffness coefficients given by Eqs. (A.1)–(A.8) are then reduced to

$$k_{p1} = -\mu\pi\int_{r_1}^{r_2}\left(\delta_2(r) + \sum_{i=1}^{n}\delta_{4(i)}(r)\cos(\omega_i t)\right)r^2\partial r, \tag{37}$$

$$k_{p2} = 2\pi\int_{r_1}^{r_2}\left(\delta_1(r) - \delta_2(r)s_{\text{nom}} + \sum_{i=1}^{n}(\delta_{3(i)}(r) - \delta_{4(i)}(r)s_{\text{nom}})\cos(\omega_i t)\right)r\,\partial r, \tag{38}$$

$$k_{p3} = -k_{p2}, \tag{39}$$

$$k_{p4} = k_{p1}, \tag{40}$$

$$k_{p5} = \pi\int_{r_1}^{r_2}\left(\delta_2(r) + \sum_{i=1}^{n}\delta_{4(i)}(r)\cos(\omega_i t)\right)r^3\partial r, \tag{41}$$

$$k_{p6} = 2\pi\mu\int_{r_1}^{r_2}\left(\delta_1(r) - \delta_2(r)s_{\text{nom}} + \sum_{i=1}^{n}(\delta_{3(i)}(r) - \delta_{4(i)}(r)s_{\text{nom}})\cos(\omega_i t)\right)r^2\partial r, \tag{42}$$

$$k_{p7} = -k_{p6}, \tag{43}$$

$$k_{p8} = k_{p5} \tag{44}$$

while the external loads given by Eqs. (A.9)–(A.12) become zero, i.e.

$$\mathbf{f}_p = \begin{bmatrix}0 & 0 & 0 & 0\end{bmatrix}^{\mathrm{T}}. \tag{45}$$

3.2.4. Derivation of the load model when gap dependency of the oscillating parts is excluded

From the measurements presented in this paper, it could not be stated if the oscillating parts of the pressure also vary with the gap. If these variations are negligible the pressure distribution reduces to

$$p = (\delta_1(r,\eta) - \delta_2(r,\eta)s) + \left(\sum_{i=1}^{n}\delta_{3(i)}(r,\eta)\cos(\omega_i t)\right). \tag{46}$$

The stiffness coefficients given by Eqs. (A.1)–(A.8) reduce to,

$$k_{p1} = -\mu\int_0^{2\pi}\int_{r_1}^{r_2}\delta_2(r,\eta)r^2\sin^2(\eta)\partial r\,\partial\eta, \tag{47}$$

$$k_{p2} = \int_0^{2\pi}\int_{r_1}^{r_2}\left(\delta_1(r,\eta) - \delta_2(r,\eta)(s_{\text{nom}} - \mu r\,\cos(\eta)\sin(\eta)) + \sum_{i=1}^{n}\delta_{3(i)}(r,\eta)\cos(\omega_i t)\right)r\,\partial r\,\partial\eta, \tag{48}$$

$$k_{p3} = -\int_0^{2\pi}\int_{r_1}^{r_2}\left(\delta_1(r,\eta) - \delta_2(r,\eta)(s_{\text{nom}} + \mu r\,\cos(\eta)\sin(\eta)) + \sum_{i=1}^{n}\delta_{3(i)}(r,\eta)\cos(\omega_i t)\right)r\,\partial r\,\partial\eta, \tag{49}$$

$$k_{p4} = -\mu\int_0^{2\pi}\int_{r_1}^{r_2}\delta_2(r,\eta)r^2\cos^2(\eta)\partial r\,\partial\eta, \tag{50}$$

$$k_{p5} = \int_0^{2\pi} \int_{r_1}^{r_2} \delta_2(r,\eta) r^3 \sin^2(\eta) \partial r \, \partial \eta, \tag{51}$$

$$k_{p6} = \int_0^{2\pi} \int_{r_1}^{r_2} \left(\mu\delta_1(r,\eta) - \delta_2(r,\eta)(\mu s_{\text{nom}} + r\,\cos(\eta)\sin(\eta)) + \sum_{i=1}^{n} \mu\delta_{3(i)}(r,\eta)\cos(\omega_i t) \right) r^2 \partial r \, \partial \eta, \tag{52}$$

$$k_{p7} = -\int_0^{2\pi} \int_{r_1}^{r_2} \left(\mu\delta_1(r,\eta) - \delta_2(r,\eta)(\mu s_{\text{nom}} - r\,\cos(\eta)\sin(\eta)) + \sum_{i=1}^{n} \mu\delta_{3(i)}(r,\eta)\cos(\omega_i t) \right) r^2 \partial r \, \partial \eta, \tag{53}$$

$$k_{p8} = \int_0^{2\pi} \int_{r_1}^{r_2} \delta_2(r,\eta) r^3 \cos^2(\eta) \partial r \, \partial \eta. \tag{54}$$

The external loads given by Eqs. (A.9)–(A.12) reduces to,

$$f_{pX} = \mu \left(\int_0^{2\pi} \int_{r_1}^{r_2} \left(\delta_1(r,\eta) - \delta_2(r,\eta) s_{\text{nom}} + \sum_{i=1}^{n} \delta_{3(i)}(r,\eta)\cos(\omega_i t) \right) r\,\sin(\eta) \partial r \, \partial \eta \right), \tag{55}$$

$$f_{pY} = -\mu \left(\int_0^{2\pi} \int_{r_1}^{r_2} \left(\delta_1(r,\eta) - \delta_2(r,\eta) s_{\text{nom}} + \sum_{i=1}^{n} \delta_{3(i)}(r,\eta)\cos(\omega_i t) \right) r\,\cos(\eta) \partial r \, \partial \eta \right), \tag{56}$$

$$f_{p\varphi} = -\int_0^{2\pi} \int_{r_1}^{r_2} \left(\delta_1(r,\eta) - \delta_2(r,\eta) s_{\text{nom}} + \sum_{i=1}^{n} \delta_{3(i)}(r,\eta)\cos(\omega_i t) \right) r^2\,\sin(\eta) \partial r \, \partial \eta, \tag{57}$$

$$f_{p\theta} = \int_0^{2\pi} \int_{r_1}^{r_2} \left(\delta_1(r,\eta) - \delta_2(r,\eta) s_{\text{nom}} + \sum_{i=1}^{n} \delta_{3(i)}(r,\eta)\cos(\omega_i t) \right) r^2\,\cos(\eta) \partial r \, \partial \eta. \tag{58}$$

4. Numerical results

When the process is applied, Eq. (5) is extended by the stiffness matrix $\mathbf{K}_p(t)$ and the external load vector $\mathbf{f}_p(t)$ to

$$\mathbf{M}\ddot{\mathbf{X}} + (\mathbf{C} + \Omega\mathbf{G})\dot{\mathbf{X}} + (\mathbf{K}_s + \mathbf{K}_p(t))\mathbf{X} = \mathbf{f}_u(t) + \mathbf{f}_p(t). \tag{59}$$

This equation of motion is a linear ordinary differential equation with time-dependant coefficients, thus general analytical closed-form solutions cannot be found by known methods. However, by numerical simulations the time evolution can be derived. To illustrate the consequences of rotordynamics when the process is applied, numerical simulations will thus be used. The derived general pressure distribution (see Section 3.2.1) will be used here. For simplicity, only one frequency component will be considered for the time-dependant part of the load model, and both inlet and outlet pressures are set to zero. The functions $\delta_{1-4(1)}$ are further assumed to be

$$\delta_{1-4(1)} = a_{1-4}\delta_c, \tag{60}$$

where a_{1-4} are constants and δ_c is a common pressure distributions function. By combining Eqs. (23)–(26) and Eq. (62) the constants

$$a_1 = \gamma_1 \Big/ \int_0^{2\pi} \int_{r_1}^{r_2} r\delta_c(r,\eta) \partial r \, \partial \eta, \quad a_2 = \gamma_2 \Big/ \int_0^{2\pi} \int_{r_1}^{r_2} r\delta_c(r,\eta) \partial r \, \partial \eta,$$
$$a_3 = \lambda_{3(1)} \Big/ \int_0^{2\pi} \int_{r_1}^{r_2} r\delta_c(r,\eta) \partial r \, \partial \eta \text{ and } a_4 = \gamma_{4(1)} \Big/ \int_0^{2\pi} \int_{r_1}^{r_2} r\delta_c(r,\eta) \partial r \, \partial \eta. \tag{61–64}$$

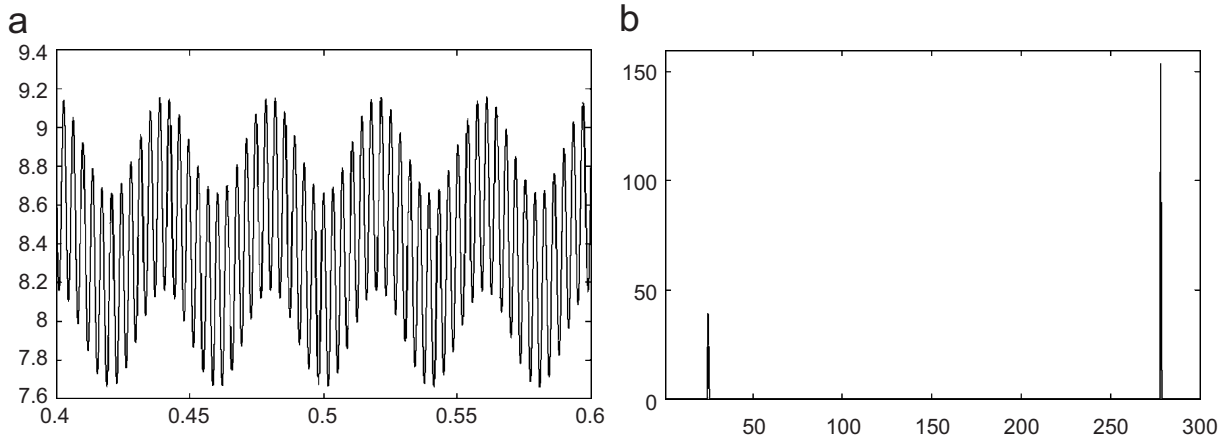

Fig. 6. (a) Time evolution in X-direction and (b) corresponding FFT.

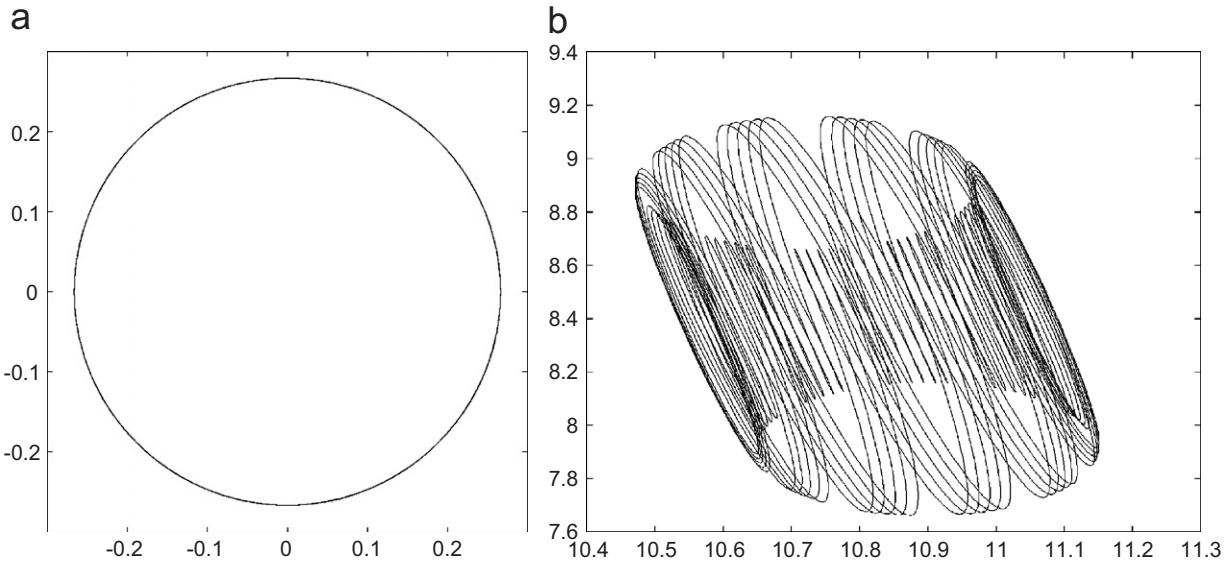

Fig. 7. Orbits in the XY-plane for (a) only unbalance and (b) process load model included.

Measurements were conducted [16] that showed the radial shear force to increase from the inlet of the refining zone before passing a maximum and finally decreasing. However, no reports about the circumferential distribution exist. Hence, the common pressure distribution is assumed to be

$$\delta_c = (1 - \cos(2\pi(r - r_1)/(r_2 - r_1)))(1 + \sin(\eta)) \tag{65}$$

which is a non-axisymmetric distribution.

Inserting Eqs. (60)–(65) into Eqs. (A.1)–(A.12) results in expressions for the stiffness coefficients and external load coefficients that can be solved.

For the numerical analyses, the set of parameters $\Omega = 25\,(\mathrm{Hz})$, $\omega_1 = 278\,(\mathrm{Hz})$, $m = 2778\,(\mathrm{kg})$, $P = 5 \times 10^6\,(\mathrm{W})$, $J_p = 976\,(\mathrm{kg\,m^2})$, $J_t = 488\,(\mathrm{kg\,m^2})$, $\zeta_1 = \zeta_2 = 0.1$, $k_{11} = 5.25 \times 10^8\,(\mathrm{N/m})$, $k_{12} = k_{21} = 1.58 \times 10^8\,(\mathrm{N/rad})$, $k_{22} = 1.11 \times 10^8\,(\mathrm{N\,m/rad})$, $\varepsilon = 1.00 \times 10^{-5}\,(\mathrm{m})$, $\gamma_1 = 1.60 \times 10^6\,(\mathrm{N})$, $\gamma_2 = 1.00 \times 10^8\,(\mathrm{N/m})$,

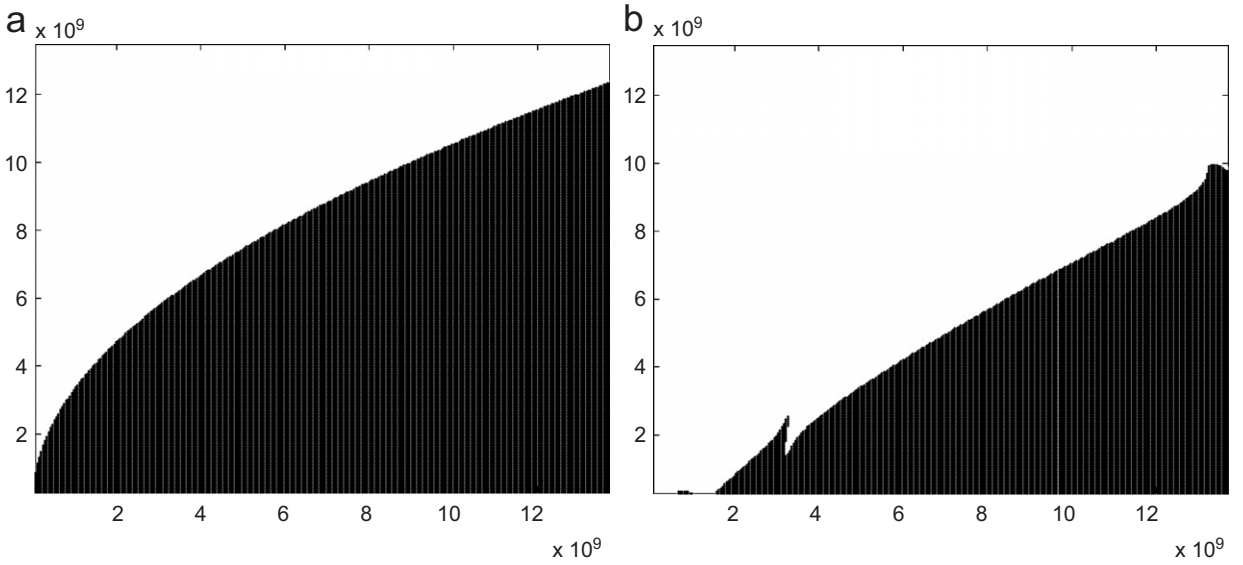

Fig. 8. Stability charts: (a) without process load model and (b) with process load model.

$\gamma_{3(1)} = 2.10 \times 10^3$ (N), $\gamma_{4(1)} = 2.00 \times 10^8$ (N/m), $r_1 = 0.1$ (m), $r_2 = 0.8$ (m) and $s_{\text{nom}} = 5.00 \times 10^{-3}$ (m) is used. The initial conditions for all simulations are set to zero.

Fig. 6(a) shows the time evolution in the X-direction when the process load model has been applied. The corresponding FFT-diagram in Fig. 6(b) shows peaks for the spin speed as well as for the process frequency.

Fig. 7(a) shows the whirling orbit in the XY-plane at idle (unbalance response) and Fig. 7(b) shows the corresponding whirling motion when the process load model is applied.

Because the homogenous part of the equation of motion is non-autonomous the stability cannot be analysed by means of eigenvalues. However, the time dependency in this numerical example is periodic, i.e. the Floquet theory [20] can be used. To make the effect of the time dependency more significant, the power in this case is increased to $P = 10 \times 10^6$ (W) and the damping decreased to $\zeta_1 = \zeta_2 = 0.01$. Fig. 8 illustrates stability charts when k_{11} and k_{12} are varied; black means stable vibration and white unstable. Fig. 8(a) shows the situation at idle while Fig. 8(b) includes the process load model in the analysis.

5. Discussion and conclusions

The aim of this paper is to suggest a load model for the fibre refining process to be used in the product development of such machines. The strategy is to fit a pressure distribution into axial force measurements.

From Fig. 1, it can be concluded that a significant time dependency in the axial force on the rotor exists due to the process for a specific refiner. Fig. 1 shows that this axial force can be divided into one constant part (compared to the vibration amplitude within the measured time), and a superimposed oscillating part with different frequencies.

Fig. 2 shows how the constant part of the axial force changes with the nominal gap. From this figure it can be concluded that a linear dependency can be used as an approximate model for the constant part of the axial process load (see Eq. (2)).

From the DFT shown in Fig. 3, an uncertain coupling between the nominal gap and the oscillating part of the load can be found. Hence, both no dependency and linear dependency on the gap are discussed in this paper. As well, the effects of phase differences of the process load are neglected.

Combining the constant and oscillating parts result in an approximate expression of the axial process force (see Eq. (4)).

An ordinary four dof model is used to discuss how the process is introduced in the rotordynamical calculations (see Section 3.1). The process models concern variations of the gap inside the refining zone,

meaning that translations in the X and Y directions will not lead to any change of process load (they do not change this gap), which explains why the two leftmost columns in the process stiffness matrices (see for example Eq. (29)) are zero. Since no unique pressure distribution fits the axial process force, four different cases are presented.

In the general case, the pressure distribution depends on the radial position and angle on the rotor (see Eq. (18)). Such pressure leads to an oscillating stiffness matrix and oscillating external loads in all four dof, meaning that even if the rotor is completely balanced the process will still excite all dof. Therefore, it can be concluded that for the general pressure distribution the process frequencies (included in the oscillating part) must be considered in the design so that, for example, they do not coincide with the eigenfrequencies. All the stiffness coefficients, $k_{p1} - k_{p8}$, differ from each other and all are time dependant; hence, the corresponding stiffness matrix becomes non-symmetrical and time dependant. Because the time dependency may consist of many frequency components, the process stiffness matrix does not necessarily have to be periodic. On the contrary, depending on the ratio between the components, it can also be quasi-periodic.

When the process is treated as distributed springs the number of different stiffness coefficients are reduced to six, since $k_{p2} = k_{p3}$ and $k_{p6} = k_{p7}$ (see Eqs. (32)–(35)). Even for this case all stiffness coefficients consist of an oscillating part. The external load vector remains the same as with the general pressure distribution case.

When the angular pressure variation is constant, the number of different stiffness coefficients is reduced to four (since $k_{p2} = -k_{p3}$, $k_{p4} = k_{p1}$, $k_{p6} = -k_{p7}$ and $k_{p8} = k_{p5}$), though they all depend on time (see Eqs. (37)–(44)). The external load vector becomes zero in this case, which is considered an advantage for design purposes. The process frequencies vanish from the right side of the e.o.m., meaning that they will not lead to resonance problems.

The last example of the pressure distribution is if the oscillating part does not depend on the gap. From Eqs. (47)–(54), the number of different stiffness coefficients does not decrease. However, the coefficients k_{p1}, k_{p4}, k_{p5} and k_{p8} do not depend on time. The external loads will still act in all directions and still oscillate (see Eqs. (55)–(58)).

Note that combining the cases of distributed springs together with excluded angular pressure variations leads to the conditions $k_{p2} = k_{p3} = 0$ and $k_{p6} = k_{p7} = 0$. If, besides this combination, the oscillating part does not depend on the gap, the remaining four stiffness coefficients become constant. This means that the homogenous part of the governing equation of motion would be autonomous; therefore, the dynamics are known from the theory of linear systems with constant coefficients. This situation is strived for when designing new refiners, since the dynamics can be predicted within the needed accuracy. How this situation is realised in practice is yet to be uncovered. However, this paper shows the potential of refiners that lead to this kind of pressure distribution in production.

From Fig. 6, it can be stated that for the specific set of parameters the rotor model vibrates with the fundamental frequencies Ω (spin speed) and ω_1 (process speed). Fig. 7 shows that when the process model is applied the whirling orbit in the XY-plane deviates from the circular unbalance response (see Fig. 7(a)). Besides deviation by means of shape, the orbit is also displaced from the origin. It is important to control this kind of static deflection due to the small gap between the stator and rotor in fibre refiners ($\sim$0.5 mm). By comparing Fig. 8(a) and (b) it can be concluded that the unstable domain increases when the process load model is applied. Notice that when this load is excluded, the system is stable for $k_{11}k_{22} > k_{12}^2$ [21], which gives the black area in Fig. 8(a).

It should be stated that the results presented in this paper are derived from measurements on a specific refiner with a specific process. To generalise this model additional validation measurements have to be made. The idea in this paper was to introduce basic dynamical features that may arise inside the refining zone when the machine produces fibre. Even though the models are derived for refiners, the generality of the model makes them suitable for a wide range of different applications. Finally, after additional measurements it is likely that the derived process load model can be used in product development to evaluate the dynamics of refiner concepts.

Acknowledgement

The present work is a project in the Polhem Laboratory at Luleå University of Technology, one of VINNOVA's (the Swedish Agency for Innovation Systems) competence centra.

Appendix A. Process stiffness coefficients and external load

$$k_{p1} = -\mu \int_0^{2\pi} \int_{r_1}^{r_2} \left(\delta_2(r,\eta) + \sum_{i=1}^{n} \delta_{4(i)}(r,\eta)\cos(\omega_i t) \right) r^2 \sin^2(\eta) \partial r \, \partial \eta, \tag{A.1}$$

$$k_{p2} = \int_0^{2\pi} \int_{r_1}^{r_2} (\delta_1(r,\eta) - \delta_2(r,\eta)(s_{\text{nom}} - \mu r \cos(\eta)\sin(\eta)) + \sum_{i=1}^{n} (\delta_{3(i)}(r,\eta) - \delta_{4(i)}(r,\eta)(s_{\text{nom}} - \mu r \cos(\eta)\sin(\eta)))\cos(\omega_i t) \Big) r \, \partial r \, \partial \eta, \tag{A.2}$$

$$k_{p3} = -\int_0^{2\pi} \int_{r_1}^{r_2} (\delta_1(r,\eta) - \delta_2(r,\eta)(s_{\text{nom}} + \mu r \cos(\eta)\sin(\eta)) + \sum_{i=1}^{n} (\delta_{3(i)}(r,\eta) - \delta_{4(i)}(r,\eta)(s_{\text{nom}} + \mu r \cos(\eta)\sin(\eta)))\cos(\omega_i t) \Big) r \, \partial r \, \partial \eta, \tag{A.3}$$

$$k_{p4} = -\mu \int_0^{2\pi} \int_{r_1}^{r_2} \left(\delta_2(r,\eta) + \sum_{i=1}^{n} \delta_{4(i)}(r,\eta)\cos(\omega_i t) \right) r^2 \cos^2(\eta) \partial r \, \partial \eta, \tag{A.4}$$

$$k_{p5} = \int_0^{2\pi} \int_{r_1}^{r_2} \left(\delta_2(r,\eta) + \sum_{i=1}^{n} \delta_{4(i)}(r,\eta)\cos(\omega_i t) \right) r^3 \sin^2(\eta) \partial r \, \partial \eta, \tag{A.5}$$

$$k_{p6} = \int_0^{2\pi} \int_{r_1}^{r_2} (\mu\delta_1(r,\eta) - \delta_2(r,\eta)(\mu s_{\text{nom}} + r \cos(\eta)\sin(\eta)) + \sum_{i=1}^{n} \mu\delta_{3(i)}(r,\eta) - \delta_{4(i)}(r,\eta)(\mu s_{\text{nom}} + r \cos(\eta)\sin(\eta))\cos(\omega_i t) \Big) r^2 \partial r \, \partial \eta, \tag{A.6}$$

$$k_{p7} = -\int_0^{2\pi} \int_{r_1}^{r_2} (\mu\delta_1(r,\eta) - \delta_2(r,\eta)(\mu s_{\text{nom}} - r \cos(\eta)\sin(\eta)) + \sum_{i=1}^{n} \mu\delta_{3(i)}(r,\eta) - \delta_{4(i)}(r,\eta)(\mu s_{\text{nom}} - r \cos(\eta)\sin(\eta))\cos(\omega_{pi} t) \Big) r^2 \partial r \, \partial \eta, \tag{A.7}$$

$$k_{p8} = \int_0^{2\pi} \int_{r_1}^{r_2} \left(\delta_2(r,\eta) + \sum_{i=1}^{n} \delta_{4(i)}(r,\eta)\cos(\omega_i t) \right) r^3 \cos^2(\eta) \partial r \, \partial \eta, \tag{A.8}$$

$$f_{pX} = \mu \left(\int_0^{2\pi} \int_{r_1}^{r_2} \left(\delta_1(r,\eta) - \delta_2(r,\eta) s_{\text{nom}} + \sum_{i=1}^{n} (\delta_{3(i)}(r,\eta) - \delta_{4(i)}(r,\eta) s_{\text{nom}})\cos(\omega_i t) \right) r \sin(\eta) \partial r \, \partial \eta \right), \tag{A.9}$$

$$f_{pY} = -\mu \left(\int_0^{2\pi} \int_{r_1}^{r_2} \left(\delta_1(r,\eta) - \delta_2(r,\eta) s_{\text{nom}} + \sum_{i=1}^{n} (\delta_{3i}(r,\eta) - \delta_{4(i)}(r,\eta) s_{\text{nom}})\cos(\omega_i t) \right) r \cos(\eta) \partial r \, \partial \eta \right), \tag{A.10}$$

$$f_{p\varphi} = -\int_0^{2\pi}\int_{r_1}^{r_2}\left(\delta_1(r,\eta) - \delta_2(r,\eta)s_{\text{nom}} + \sum_{i=1}^{n}(\delta_{3(i)}(r,\eta) - \delta_{4(i)}(r,\eta)s_{\text{nom}})\cos(\omega_i t)\right) r^2\,\sin(\eta)\partial r\,\partial\eta, \tag{A.11}$$

$$f_{p\theta} = \int_0^{2\pi}\int_{r_1}^{r_2}\left(\delta_1(r,\eta) - \delta_2(r,\eta)s_{\text{nom}} + \sum_{i=1}^{n}(\delta_{3(i)}(r,\eta) - \delta_{4(i)}(r,\eta)s_{\text{nom}})\cos(\omega_i t)\right) r^2\,\cos(\eta)\partial r\,\partial\eta. \tag{A.12}$$

References

[1] T. Yamamoto, Y. Ishida, *Linear and Nonlinear Rotordynamics a Modern Treatment with Applications*, Wiley, New York, 2001.

[2] J.-J. Sinou, F. Thouverez, L. Jezequel, Non-linear analysis of a complex rotor/stator contact system, *Journal of Sound and Vibration* 278 (2004) 1095–1129.

[3] H.S. Kim, M. Cho, S.J. Song, Stability analysis of a turbine rotor system with Alford forces, *Journal of Sound and Vibration* 258 (2002) 777–790.

[4] A.F. Storace, D.C. Wisler, H.-W. Shin, B.F. Beacher, F.F. Ehrich, Z.S. Spakovszky, M. Martinez-Sanchez, S.J. Song, Unsteady flow and whirl-inducing forces in axial-flow compressors: part I—experiment, *Journal of Turbomachinery* 123 (2001) 433–445.

[5] F.F. Ehrich, Z.S. Spakovszky, M. Martinez-Sanchez, S.J. Song, D.C. Wisler, A.F. Storace, H.-W. Shin, B.F. Beacher, Unsteady flow and whirl-inducing forces in axial-flow compressors: part II—analysis, *Journal of Turbomachinery* 123 (2001) 433–445.

[6] C.M. Myllerup, G. Keith, Whirl frequency dependent Alford forces in axial compressors, *Proceedings of the ASME Turbo Expo*, Vienna, Austria, June 14–17, 2004, pp. 581–592.

[7] K.B. Miles, W.D. May, The flow of pulp in chip refiners, *Journal of Pulp and Paper Science* 16 (1990) 63–72.

[8] J.C. Roux, T.L. Mayade, Modeling of the particle breakage kinetics in the wet mills for the paper industry, *Powder Technology* 105 (1999) 237–242.

[9] S. Holmberg, K. Persson, H. Petersson, Nonlinear mechanical behaviour and analysis of wood and fibre materials, *Computer and Structures* 72 (1999) 459–480.

[10] D. Di Ruscio, J.G. Balchen, A state space model for the wood chip refining process, *Journal of Pulp and Paper Science* 22 (1996) 104–112.

[11] R. Amiri, R. Hofmann, Dynamic compressibility of papermaking pulps, *Paper and Timber* 85 (2003) 100–106.

[12] R. Whalley, D. Mitchell, Pulp refining at resonance, *Mechanical Systems and Signal Processing* 13 (1999) 643–665.

[13] W.C. Frazier, Applying hydrodynamic lubrication theory to predict refiner behaviour, *Journal of Pulp and Paper Science* 14 (1988) 1–5.

[14] P.-L. Jiang, L. Yu, Effect of a hydrodynamic thrust bearing on the statics and dynamics of a rotor-bearing system, *Mechanics Research Communications* 25 (1998) 219–224.

[15] D. Ouellet, R. Weiss, Modeling of the nonlinear axial vibrations of the rotor assembly in a disc refiner, *Journal of Pulp and Paper Science* 20 (1994) 259–265.

[16] H.-O. Backlund, H. Höglund, P. Gradin, Study of tangential forces and temperature profiles in commercial refiners, *Proceedings in IMPC*, Quebec City, June 2–5, 2003, pp. 379–386.

[17] J. Senger, A. Siadat, D. Ouellet, P. Wild, Measurement of normal and shear forces during refining using a piezoelectric force sensor, *Proceedings of the International Mechanical Pulping Conference*, 2003, pp. 403–407.

[18] J. Senger, M. Olmstead, D. Ouellet, P. Wild, Measurement of normal and shear forces in the refining zone of a tmp refiner, *PAPTAC 90th Annual Meeting*, 2004, pp. 17–21.

[19] G. Genta, C. Delprete, E. Busa, Some considerations on the basic assumptions in rotordynamics, *Journal of Sound and Vibration* 227 (1999) 611–645.

[20] R.M.M. Mattheij, J. Molenaar, *Ordinary Differential Equations in Theory and Practice*, Wiley, Chichester, 1996.

[21] M. Karlberg, J.-O. Aidanpää, Evaluation of rotordynamical concepts subjected to rotating unbalance and impulse, *Proceedings of the Sixth International Conference on Rotor Dynamics*, 2002, pp. 752–758.